On the validity of the planar wave approximation to compute synthetic seismograms of teleseismic body waves in a 3-D regional model

Vadim Monteiller, Stephen Beller, Bastien Plazolles, Sébastien Chevrot

submitted to *Geophysical Journal International*

On the validity of the planar wave approximation to compute synthetic seismograms of teleseismic body waves in a 3-D regional model

Vadim Monteiller[1], Stephen Beller[2,3], Bastien Plazolles[2], and Sébastien Chevrot[2]

[1] *LMA, CNRS, UPR 7051, Aix-Marseille University, Centrale Marseille, 13402 Marseille Cedex 20, France.*

[2] *GET, UMR 5563, Observatoire Midi Pyrenees, Université Paul Sabatier, CNRS, IRD, Toulouse, France.*

[3] *Department of Geosciences, Princeton University, Guyot Hall, Princeton, NJ 08544, USA.*

24 November 2020

SUMMARY

Injection methods are a very efficient means to compute synthetic seismograms of short period teleseismic body waves in 3D regional models. The principle is to inject an incident teleseismic wavefield inside a regional 3D cartesian spectral-element grid. We have developed an open source package which allows us to inject either an incident plane wave, computed with a frequency-wavenumber method, or the complete wavefield computed in a spherically symmetric reference Earth model with AxiSEM. The computations inside the regional spectral-element grid are performed with SPECFEM3D_Cartesian. We compare the efficiency and reliability of the two injection methods for teleseismic P waves, considering a wide range of epicentral distance and hypocentral depths. Our simulations demonstrate that in practice the effects of wavefront and Earth curvature are negligible for moderate size regional domains (several hundreds of kilometers) and for periods larger than 2 s. The main differences observed in synthetic seismograms are related to secondary phases that have a different slowness from the one of the reference P phase.

Key words: Computational seismology – Wave propagation – Body waves – Waveform inversion – Seismic tomography.

1 INTRODUCTION

The computation of accurate synthetic seismograms in 3D Earth models is a major challenge of modern seismology, with important prospects for both source and structural studies. While numerical methods have been developed to simulate the propagation of elastic waves in 3D Earth models (Komatitsch & Tromp 2002), these methods still suffer from a high computational cost, which limits their applications to relatively long periods, even with modern supercomputers (e.g Komatitsch et al. 2003).

In order to reduce the computational cost of forward modelling, a prerequisite to full waveform inversion, different groups have developed injection techniques to compute synthetic seismograms in regional 3D models (Bielak & Christiano 1984; Chevrot et al. 2004; Roecker et al. 2010; Monteiller et al. 2013; Tong et al. 2014a,b; Masson & Romanowicz 2017a,b; Beller et al. 2018a; Lin et al. 2019). The key idea is that if the regional domain is far from the source region, which is typically the case for a teleseismic source, then the problem can be separated into two distinct parts: a global propagation problem and a regional propagation problem. In this case, the time-consuming 3D computations are restricted to a small regional domain, and short period 3D wave fields can be computed efficiently with reasonable computational resources. A natural choice for the computations in the regional domain is the spectral-element method, which can handle any type of complexity that may affect the propagation of seismic waves such as the topography of the free surface and of internal discontinuities, isotropic and anisotropic heterogeneities, and attenuation. Note that injection techniques differ from pure coupling techniques (e.g. Capdeville et al. 2003), which provide the complete and exact solution within the computational domain.

The first hybrid method (Monteiller et al. 2013) relied on the Direct Solution Method (DSM) (e.g Kawai et al. 2006) to compute the incident wavefield. This approach allowed us to build a full waveform inversion (FWI) algorithm (Monteiller et al. 2015), which was applied for the very first time on teleseismic P waves to image the deep architecture of the western Pyrenees (Wang et al.

2016). While these early works were important for the maturation of FWI with teleseismic body waves, DSM involves storing and manipulating a large number of spherical harmonics coefficients, which can be tedious and introduce serious i/o bottleneck issues. The problem is particularly severe for shallow sources, which require computations up to very large angular orders. This motivated the development of a new injection technique relying on AxiSEM (Nissen-Meyer et al. 2007, 2014), which both simplifies and accelerates the algorithm (Beller et al. 2018a,b).

An even more radical choice to simplify the problem is to inject a single plane wave in the regional spectral-element domain (Tong et al. 2014a,b). In that case, most of the complexities of the incident wave field are neglected, in addition to the curvature of the wave front and of the Earth's surface. For the price of these simplifications, the computations can be made extremely efficient even at frequencies up to 10 Hz, an objective that would be extremely challenging to reach with AxiSEM. We thus decided to also develop a new, highly optimized, injection code that couples FK and SPECFEM3D_Cartesian in order to build a versatile package able to fulfill the needs of various demanding tasks for the computations of synthetic seismograms in 3D regional models. The main objective of the present study is to give a brief overview of the new injection codes that have been developed and also to explore the limitations of the FK injection approach to model and invert short period teleseismic body waveforms.

The paper is organized as follows. After outlining the basic principles of injection techniques, we describe the different components of the RegHyM package, a complete toolbox that allows seismologists to compute synthetic seismograms in a 3D regional model with SPECFEM3D_Cartesian, considering an incident wave field computed either with the AxiSEM or FK method. We detail the different steps involved in the computation of the incident wave field with both methods, emphasizing their specificities, and the different optimizations that have been implemented to reach a high computational efficiency. We then compare the two methods using a subduction model with topography of the free surface and discuss the advantages and shortcomings of FK with respect to AxiSEM.

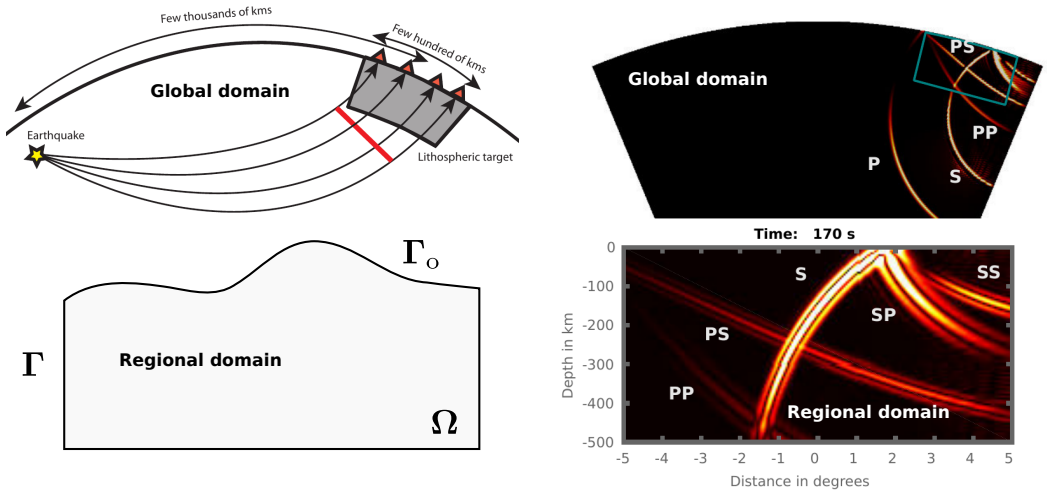

Figure 1. Injection methods consist in computing the wave field u inside a finite regional domain Ω produced by an incident wavefield u^i on its boundaries Γ.

2 INJECTION OF THE INCIDENT WAVEFIELD IN THE REGIONAL SEM GRID

2.1 Theory

The spectral-element method solves the weak form of the momentum equation (Komatitsch & Tromp 1999)

$$\int_\Omega \rho\, \mathbf{w} \cdot \partial_t^2 \mathbf{u}\, \mathrm{d}^3\mathbf{x} = \int_\Gamma \mathbf{w} \cdot (\boldsymbol{\sigma} \cdot \hat{\mathbf{n}})\, \mathrm{d}^2\mathbf{x} - \int_\Omega \boldsymbol{\nabla}\mathbf{w} : \boldsymbol{\sigma}\, \mathrm{d}^3\mathbf{x}, \tag{1}$$

where Ω designates the volume of the finite Earth model and Γ its boundary with unit outward normal $\hat{\mathbf{n}}$ (Figure 1). In this equation, ρ is the density distribution, $\mathbf{u}$ the displacement field, $\mathbf{w}$ an arbitrary test vector, and $\boldsymbol{\sigma}$ the stress tensor. A wavefield $\mathbf{u}^i$ can be injected inside a regional domain by imposing its traction wavefield $\mathbf{T}^i$ on Γ and absorbing the outgoing wavefield $\mathbf{u^s} = \mathbf{u} - \mathbf{u^i}$ produced by scattering inside the internal domain (Chevrot et al. 2004; Monteiller et al. 2013).

Imposing Stacey absorbing conditions at the model boundary Γ (Clayton & Engquist 1977; Komatitsch & Tromp 1999) leads to the following expression for the traction $\mathbf{T}$ on Γ

$$\mathbf{T} = \mathbf{T}^i + \rho V_p \left[\hat{\mathbf{n}} \cdot (\partial_t \mathbf{u} - \partial_t \mathbf{u}^i)\right] \hat{\mathbf{n}} + \rho V_s \left(\mathbf{I} - \hat{\mathbf{n}}\hat{\mathbf{n}}\right) \cdot (\partial_t \mathbf{u} - \partial_t \mathbf{u}^i)\,, \tag{2}$$

which needs to be injected in (1) to compute the displacement $\mathbf{u}$ inside Ω. From (2), we can see that the injection problem thus only requires to know $\mathbf{u}^i$ and $\mathbf{T}^i = \boldsymbol{\sigma}^i \cdot \mathbf{n}$ on the grid points located

on Γ. These two fields can be computed with any external code. In the RegHyM package, we have implemented the injection of external wave fields computed with AxiSEM (Nissen-Meyer et al. 2014) and the frequency-wavenumber (FK) method (e.g. Takeuchi & Saito 1972; Zhu & Rivera 2002).

2.2 Injection of an incident wave field computed with AxiSEM

In order to get accurate approximations of incoming teleseismic wavefields, the solver used to generate the external wavefield must honor global scale seismic wave propagation as effectively as possible. To this end, one could naturally consider 3D global seismic solvers such as SPECFEM3D_GLOBE and capture the full complexity of global seismic wavefields. While such a strategy can currently be followed to compute global synthetic seismograms down to periods of about 5 s, it is currently still too prohibitive for multiple global seismic waves simulations at lower periods.

Fortunately, the numerical complexity of global scale simulations can be reduced with reasonable simplifying assumptions on the Earth model. Among the currently available global Earth solver, AxiSEM (Nissen-Meyer et al. 2007, 2014) is probably the most attractive and efficient one. The originality of AxiSEM is to consider axisymmetric spherical Earth models so that seismic velocities and densities are invariant by rotation around Earth's polar axis. After positioning the seismic source at the pole (i.e. on the symmetry axis) by a solid rotation, a dimensionality reduction can be achieved by removing the azimuthal dependence of the seismic wavefield. Therefore, a 3D full wavefield simulation is recast as a 2D wavefield simulation problem, enabling a one-fold reduction in computational complexity.

To describe the radiation pattern of a moment tensor source, several 2D simulation need to be performed and combined to reconstruct the complete 3D wavefield. The azimuthal dependence of seismic wavefields produced by a moment tensor source can be expressed into a finite multipole expansion with monopole ($m = 0$), dipole ($m = 1$) and quadrupole ($m = 2$) source terms. The

wavefield associated to a given polar order m can then be expressed in cylindrical coordinates as

$$\mathbf{u}_m(\mathbf{x}) = \begin{pmatrix} u_s(\tilde{\mathbf{x}}) \cos m\Phi \\ u_\Phi(\tilde{\mathbf{x}}) \sin m\Phi \\ u_z(\tilde{\mathbf{x}}) \cos m\Phi \end{pmatrix}, \tag{3}$$

where $\mathbf{x} = (s, \Phi, z)$ are the coordinates along the radial, azimuthal and symmetry axes respectively and $\tilde{\mathbf{x}} = (s, z)$ the same coordinates restricted to the 2D AxiSEM computational domain.

The full response of a seismic moment tensor is finally expressed as the linear combination of Green's functions corresponding to four elementary sources (two monopoles, one dipole and one quadrupole)

$$\mathbf{u}(\mathbf{x}, t) = \sum_{k=1}^{4} \tilde{M}_k(\Phi) \tilde{\mathbf{G}}_k(\tilde{\mathbf{x}}, t; z_s) S(t), \tag{4}$$

where $S(t)$ is the source time function, $\tilde{M}_k$ the radiation pattern of the elementary source term and $\tilde{\mathbf{G}}_k$ the 2D Green function corresponding to elementary source k (located on the symmetry axis at depth z_s). The four radiations patterns are themselves linear combinations of components of the moment tensor solution:

$$\begin{aligned} \tilde{M}_1(\Phi) &= M_{rr} \\ \tilde{M}_2(\Phi) &= (M_{\theta\theta} + M_{\Phi\Phi})/2 \\ \tilde{M}_3(\Phi) &= M_{r\theta} \cos\Phi + M_{r\Phi} \sin\Phi \\ \tilde{M}_4(\Phi) &= (M_{\theta\theta} - M_{\Phi\Phi}) \cos 2\Phi + M_{\Phi\theta} \sin 2\Phi \,, \end{aligned} \tag{5}$$

where, $\tilde{M}_1$ and $\tilde{M}_2$ are two monopole sources, $\tilde{M}_3$ a dipole source and $\tilde{M}_4$ a quadripolar source.

Once the four elemental wavefields have been computed and the seismic wavefield has been reconstructed using equation (4), it is projected back into the spherical coordinate system. Finally, by applying the inverse of the solid rotation used to put the source along the symmetry axis, we obtain the wavefield expressed in the geographic reference frame.

AxiSEM computes the solution of the wave equation in the time domain. Since the far-field displacement is proportional to the particle velocity at the source, the apparent source wavelet is the time derivative of the particle displacement imposed at the source position in the AxiSEM computations. For example, to get a far-field Gaussian wavelet, we need to impose the moment-

release time function

$$S(t) = \mathrm{erf}\left[\frac{\alpha(t-t_0)}{\tau_0}\right] \tag{6}$$

so that

$$\dot{M}(t) = \dot{S}(t) = \frac{2}{\sqrt{\pi}} \exp\left[-\frac{\alpha^2(t-t_0)^2}{\tau_0^2}\right], \tag{7}$$

where $\alpha = 3.5$ so that τ_0 corresponds to the visual width of the Gaussian.

2.3 Injection of an incident wave field computed with FK

A simpler approach is to approximate the incident wavefield by a plane wave and to compute the response of the medium described by a stack of flat homogeneous layers with the frequency-wavenumber (FK) method (e.g. Takeuchi & Saito 1972; Zhu & Rivera 2002). For a detailed description of the computation of velocities and tractions with the FK method we refer the reader to Tong et al. (2014a) and Tong et al. (2014b).

Hereafter, we will only consider teleseismic P waves, but our FK injection code is also able to handle SV or SH waves. The incident wavefield is described by the backazimuth and slowness of the wave recorded at the center of the surface edge of the regional SEM grid. For an incident P wave, the incidence angle of the incoming plane wave is obtained from

$$i = \arcsin(p \cdot V_p) \tag{8}$$

where V_p is the compressional wave velocity at the base of the SEM grid, and p the ray parameter, computed in the reference Earth model. For all the computations in this study the ak135 model (Kennett et al. 1995) has been chosen. For consistency, this reference model is also imposed on the boundary nodes of the SEM grid, with a taper zone that ensures a smooth and gradual transition from the 3D regional model inside the SEM grid to the 1D global Earth model on its boundaries.

Since in FK the wavefields are computed in the frequency domain we also need to define the source wavelet spectrum. For example, for a Gaussian wavelet, following the AxiSEM conventions, the source wavelet spectrum is given by

$$S(\omega) = \frac{\sqrt{\pi}\tau_0}{\alpha} \exp\left(-\frac{\omega^2\tau_0^2}{4\alpha^2}\right), \tag{9}$$

where τ_0 is the dominant period of the wave and $\alpha = 3.5$. Again, the constant α has been chosen so that the visual width of the Gaussian in the time domain is close to τ_0. We compute the solution up to a frequency cut-off $f_{max} = 2/\tau_0$ beyond which the energy of the source spectrum drops to values lower than 1 % of the maximum. This definition of f_{max} also holds for the first and second derivatives of the Gaussian.

The other parameter that needs to be tuned is the length of the time window T. This parameter controls the temporal aliasing of the FK solution (Mallick & Frazer 1987). Since the solutions in the time domain are computed with an inverse fast Fourier transform, we obtain T-periodic wavefields

$$\sum_{n=-\infty}^{+\infty} u(t+nT) = \frac{\Delta\omega}{2\pi} \sum_{k=-K}^{K} U(k\Delta\omega) \exp\left(-ik\Delta\omega t\right), \tag{10}$$

where $\Delta\omega = 2\pi/T$ is the frequency sampling rate and $K\Delta\omega = 2\pi f_{max}$. To prevent aliasing, we thus need to choose a small frequency interval, or a time window that is sufficiently long to capture all the arrivals with a significant amplitude. As a rule of thumb, a time window of 200 s is usually sufficient for a typical teleseismic application.

3 COMPARISON OF THE AXISEM AND FK INJECTION METHODS

The FK method is particularly efficient for teleseismic applications because, in contrast to the point source case (Zhu & Rivera 2002), the medium response only needs to be computed for a single wavenumber or slowness, defined as the slowness of the reference ray that reaches the center of the regional grid at the free surface. Another advantage of the FK method is that, in contrast to AxiSEM, the amount of computations scales linearly with the maximum frequency, and thus it is possible to reach rather high frequencies with modest computational resources. In practice, teleseismic P wavefields recorded by dense local or regional arrays show some coherence typically up to 2 Hz. While computing solutions up to these frequencies is technically feasible with AxiSEM, this would require using both very fine mesh elements and very small time steps, making these computations very time consuming.

However, the computational efficiency offered by the FK method comes at the price of in-

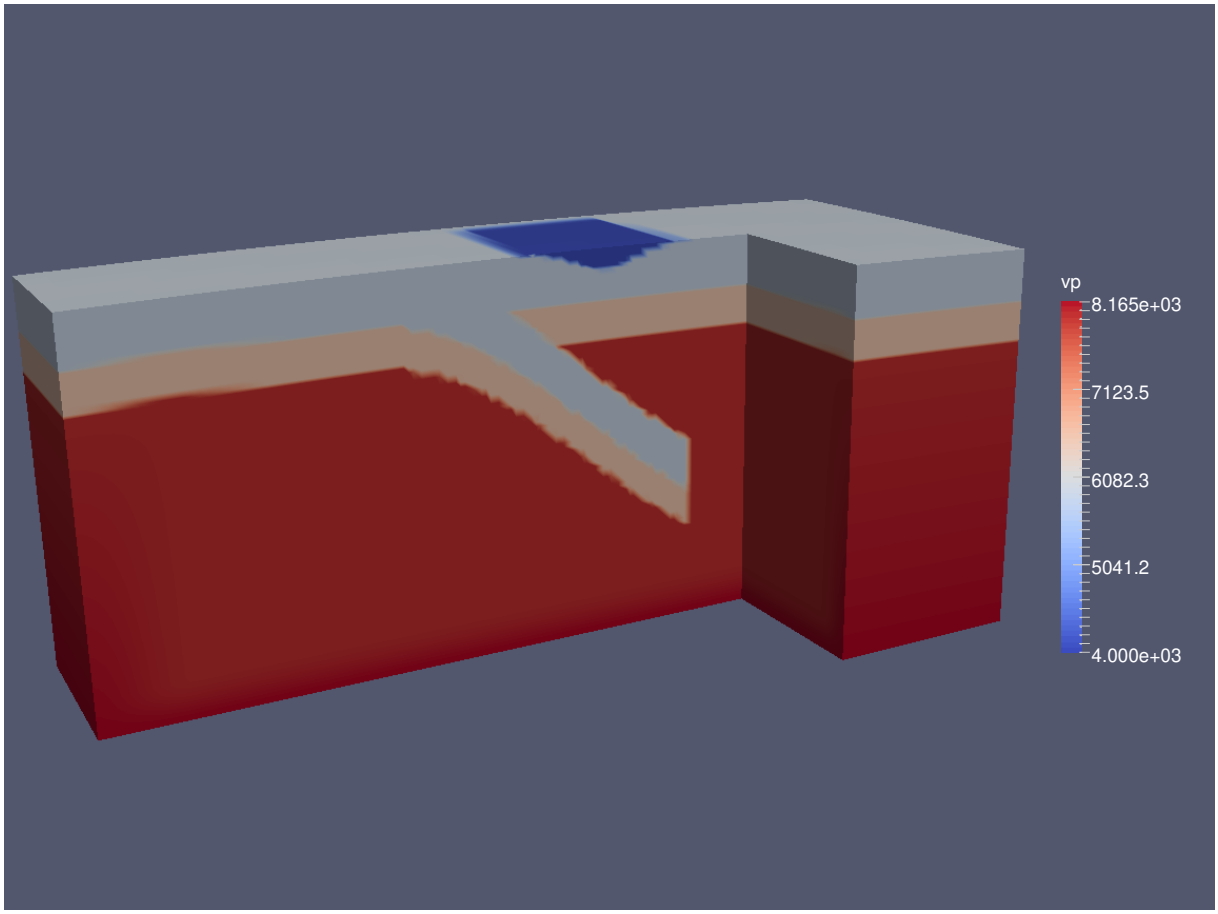

Figure 2. The subduction model used in the numerical test. We show here the model of compressional velocity Vp, expressed in m/s.

troducing some approximations in the medium response by neglecting the curvature of the wave front and of the Earth, but also the complexity of the incoming wave field, for example the secondary phases that arrive in the time window considered. In the following, we will thus investigate the limitations of the FK method for modelling teleseismic waveforms by performing numerical experiments in a continental subduction model.

3.1 Description of the numerical test

We built and meshed the 2.5D continental subduction model shown in figure 2. The dimensions of the mesh are respectively 320 km, 150 km, and 150 km, along the x, y, and z directions. The crust is composed of an upper and a lower homogenous crustal layer, lying over an homogeneous mantle. A low-velocity basin is located in the upper crust of the upper plate, on top of the conti-

	AxiSEM	FK
Mesh size SEM (km)	3.0-3.9	4.1-5.0
Number of elements SEM	114,660	69,120
Degrees of freedom SEM	7,931,572	4,936,800
Minimum resolved period (s)	1.77	1.8
Time steps SEM (s)	0.0405	0.0450
Number of time steps SEM	16,000	16,000
Computation of incident wavefields for a monopole on 96 CPU (s)	5,580	65
Computation of incident wavefields for a complete moment tensor on 96 CPU (s)	30,480	65
SEM run time on 96 CPU (s)	300	180

Table 1. Table summarizing the parameters used in the numerical tests of the AxiSEM and FK coupling methods.

nental subduction. This simple model is thus characterized by both shallow and deep strong lateral variations of seismic velocities.

The regular cartesian mesh is generated with meshfem, SPECFEM's internal mesher. We use standard Lagrange polynomials of order 4 to describe the fields inside each element along the three spatial dimensions. For the coupling with AxiSEM, the sizes of the elements range between 3.3 and 3.9 km. The number of elements is 114660, for a total of 7931572 degrees of freedom. With this mesh, the minimum resolved period is 1.77 s for a time step of 0.0405 s. The computation of the incident wavefield with AxiSEM for a dominant period of 2 s took one hour on 136 cores, while the computation of tractions and velocities on the boundary nodes of the SEM grid took 480 s on 96 cores. Note that these numbers are for a monopole source (explosion). For a complete moment tensor, the computation of the incident wavefield is 5.6 times more expensive, whereas the computation of the tractions and velocities are 4 times more expensive. In table 1, we give the numbers for both types of simulations but note that in all the simulations that are shown hereafter, a monopole source (explosion) has been used. The SEM computation time for 16000 time steps on 96 Intel CPU Skylake cores took 300 s. For the FK coupling, we use a slightly coarser mesh of 69120 elements, with sizes ranging between 4.1 and 5.0 km. The minimum resolved period is 1.8 s and the time step 0.0450 s. In that case, the number of degrees of freedom is 4936800 and the

computation time of each SEM run for 16000 time steps is about 180 s on 96 Intel CPU Skylake cores. However, the computation of the velocities and tractions on the edges of the SEM grid now only took 65 s with 96 cores.

We consider a teleseismic P wave reaching the regional grid from the south, which is recorded by a line of sensors regularly spaced along the y direction (i.e. along the down dip direction), the y axis pointing toward the north. We compute synthetic seismograms corresponding to explosion (monopole) sources located at 30° and 90° epicentral distance, and at 10 and 600 km depth (Figures 3, 4, 5, and 6). These 4 source positions describe the variability of incident teleseismic P wavefields. The shallow and deep sources allow us to explore the effects of source side complexities, and of depth phases in particular, which may have a strong imprint on seismic waveforms observed at teleseismic distances. For each case, we show the synthetic seismograms obtained with FK (left) and AxiSEM (right). The FK solution is computed for the incidence angle corresponding to the ray parameter of the incoming P wave computed in the ak135 reference Earth model (Kennett et al. 1995), using (8). Note again that this incidence angle describes the wave reaching the regional SEM grid from below and thus needs to be computed with the P wave velocity imposed at the base of the model.

3.2 Results

The upper rows of figures 3-6 show the vertical component seismograms computed for frequencies up to 0.5 Hz. Figures 3C-6C show the FK synthetic seismograms convolved by the average AxiSEM wavelet, and figures 3D-6D the AxiSEM synthetic seismograms convolved by the average FK wavelet.

The motivation for convolving the synthetic seismograms by an average wavelet is to introduce the last ingredient that is required to accurately model observed teleseismic waveforms. Indeed, natural earthquakes have a complex source time functions (usually not known), which results from the complex history of slip distribution on the fault plane. In addition, teleseismic waveforms are also contaminated by source-side propagation effects (e.g. depth phases following the main P arrival) which are mixed with the source time function to produce an apparent source time function

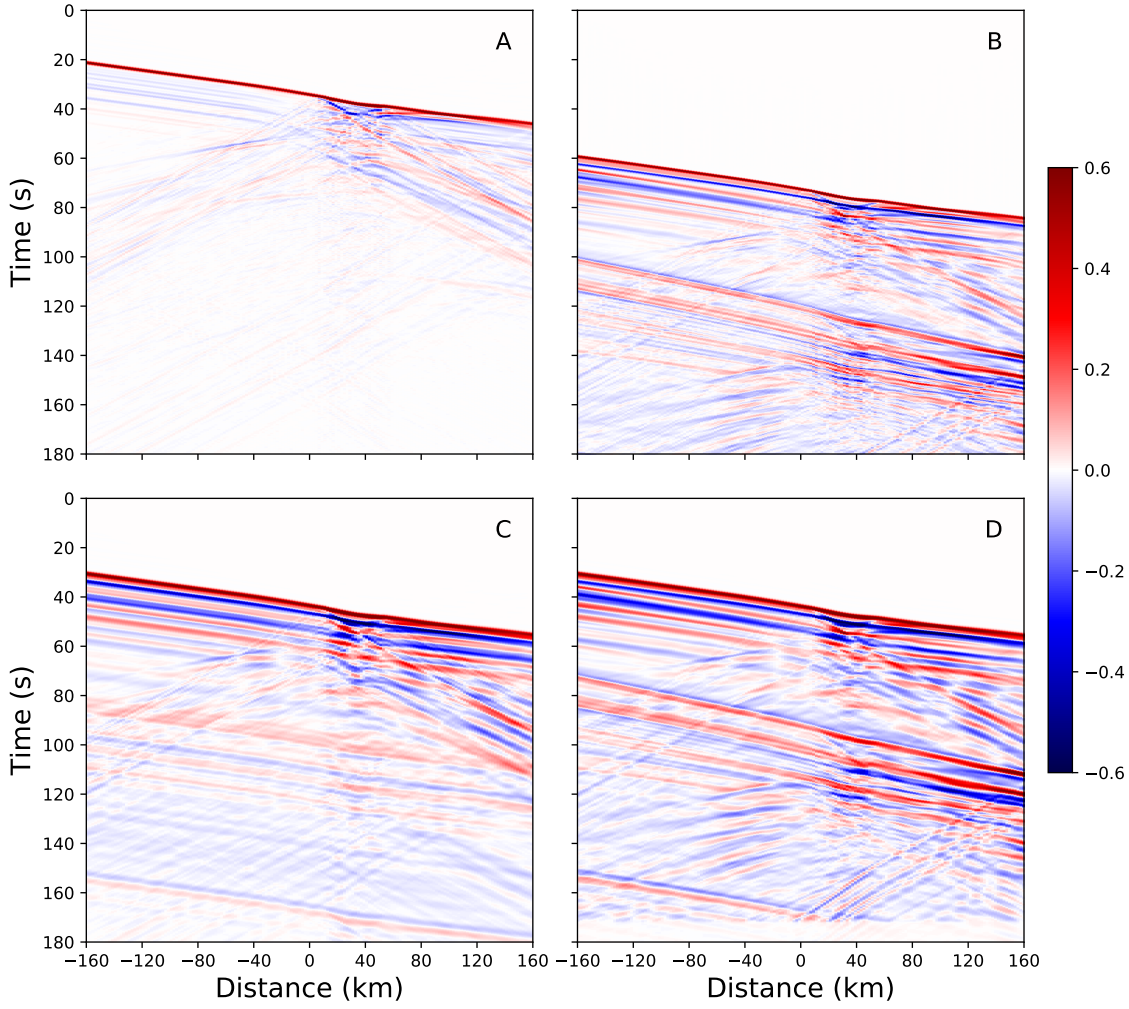

Figure 3. Vertical component of synthetic seismograms computed with FK (A) and AxiSEM (B) for a source located at an epicentral distance of 30° and 10 km depth. Same seismograms, but convolved with the average AxiSEM wavelet (C) and with the average FK wavelet (D).

or wavelet when the waves are observed far from the source region. These source wavelets can be simply estimated by aligning and stacking the vertical component P wave records of a regional seismic array. This procedure provides results very similar to principal component analysis (e.g. Rondenay 2009). Figure 7 shows the average FK and AxiSEM source wavelets corresponding to the case of a source at an epicentral distance of 30° and 10 km depth.

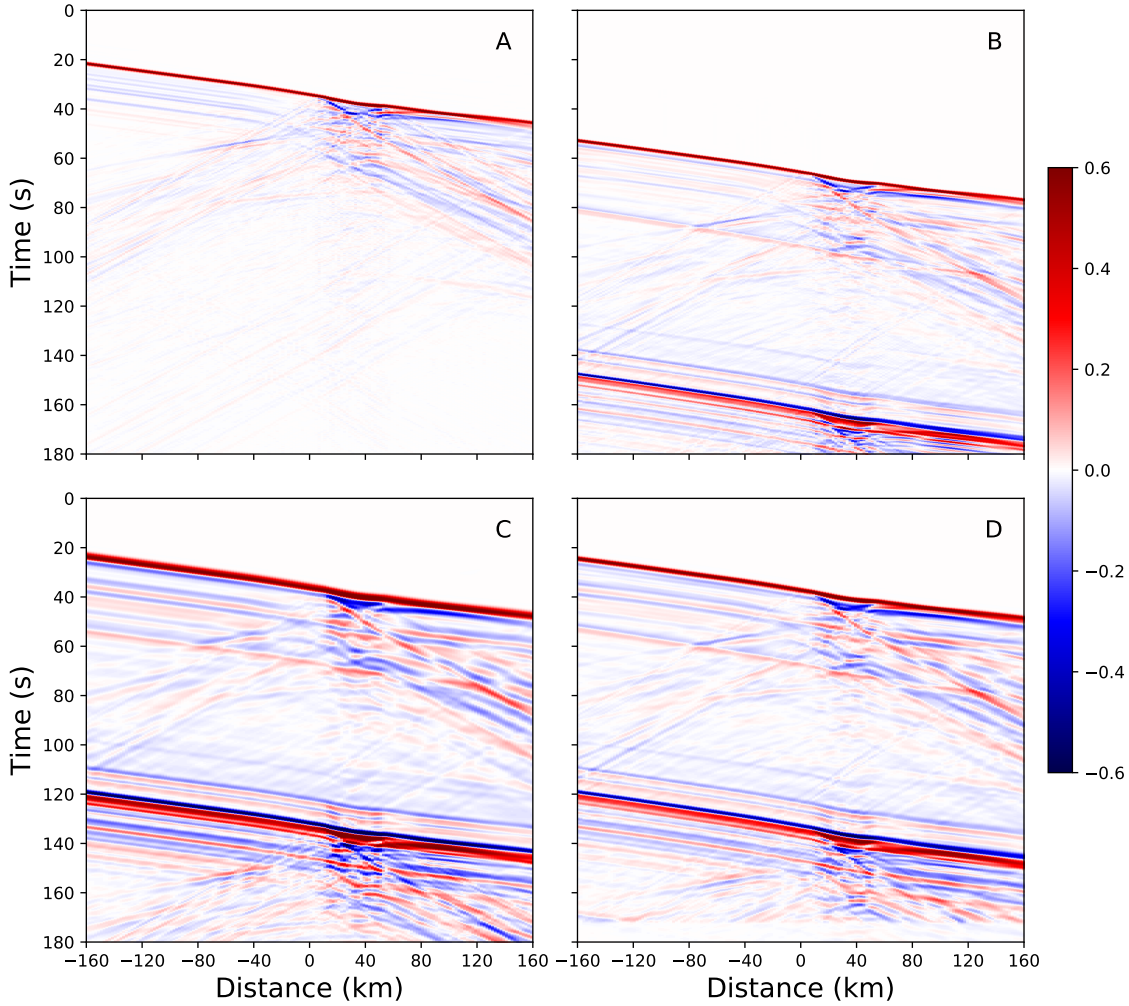

Figure 4. Same as figure 3 but for a source at 600 km depth.

3.2.1 Shallow source (hypocentral depth = 10 km)

The strongest differences between FK and AxiSEM synthetic seismograms are observed when the source is shallow (Figures 3A, 3B, and Figures 5A, 5B). In that case, since the FK method approximates the incoming wavefield with a single incident plane wave, the depth phases are not modelled. This can be clearly observed on figure 7, where the FK wavelet exhibits a clean and predominant direct P pulse, in contrast to the average AxiSEM wavelet. On the other hand, when the FK synthetics are convolved by the average AxiSEM wavelet, the differences between FK and

AxiSEM synthetics are strongly attenuated (Figures 3C, 3D, and Figures 5C, 5D). This is simply explained by the presence of depth phases in the average AxiSEM wavelet. At a distance of 30°, the only notable difference is coming from the PP wave, which arrives ∼50 s after the P wave at the center of the transect. Owing to triplications produced by the stratification of the upper mantle and transition zone, several PP phases are actually observed in this distance range. This group of phases have a slowness of about 13.6 s/°, which is much larger than the slowness of the P wave, around 8.8 s/°. Consequently, since the moveouts of PP waves are different from those of the P wave, their signature on the average AxiSEM wavelet (Figure 7, from 110 to 150 s) will only be partially captured and the convolved FK synthetic seismograms will differ from those computed with AxiSEM. At a distance of 90°, there is no secondary phase arriving in the coda of the P wave and the FK computations indeed provide an excellent approximation of the incoming teleseismic wavefield.

3.2.2 Deep source (hypocentral depth = 600 km)

For a deep source, the depth phases arrive much later and are well separated from the first P arrival. At 90° distance, the FK and AxiSEM synthetic seismograms are very similar. However, at 30° important differences are observed in the early P coda, up to 30 s after the first P arrival. These differences originate from the presence of secondary phases that have interacted with transition zone discontinuities, and which are not present in the FK computation. For example, the S660P phase, the S-to-P conversion on the 660 km discontinuity, arrives 6.5 s after the P wave. This phase has been used in the past to characterize the depression of the 660 km discontinuity beneath subduction zones (e.g. Castle & Creager 1998). Another phase that is clearly observed in the AxiSEM synthetic seismograms is p410P, a P wave that has experienced an underside reflection on the 410 km discontinuity. These secondary phases have slownesses close to the one of the P wave, and are well captured by the average wavelet estimate, which again explains why the two sets of synthetic seismograms are extremely similar after convolution by the average P wavelets.

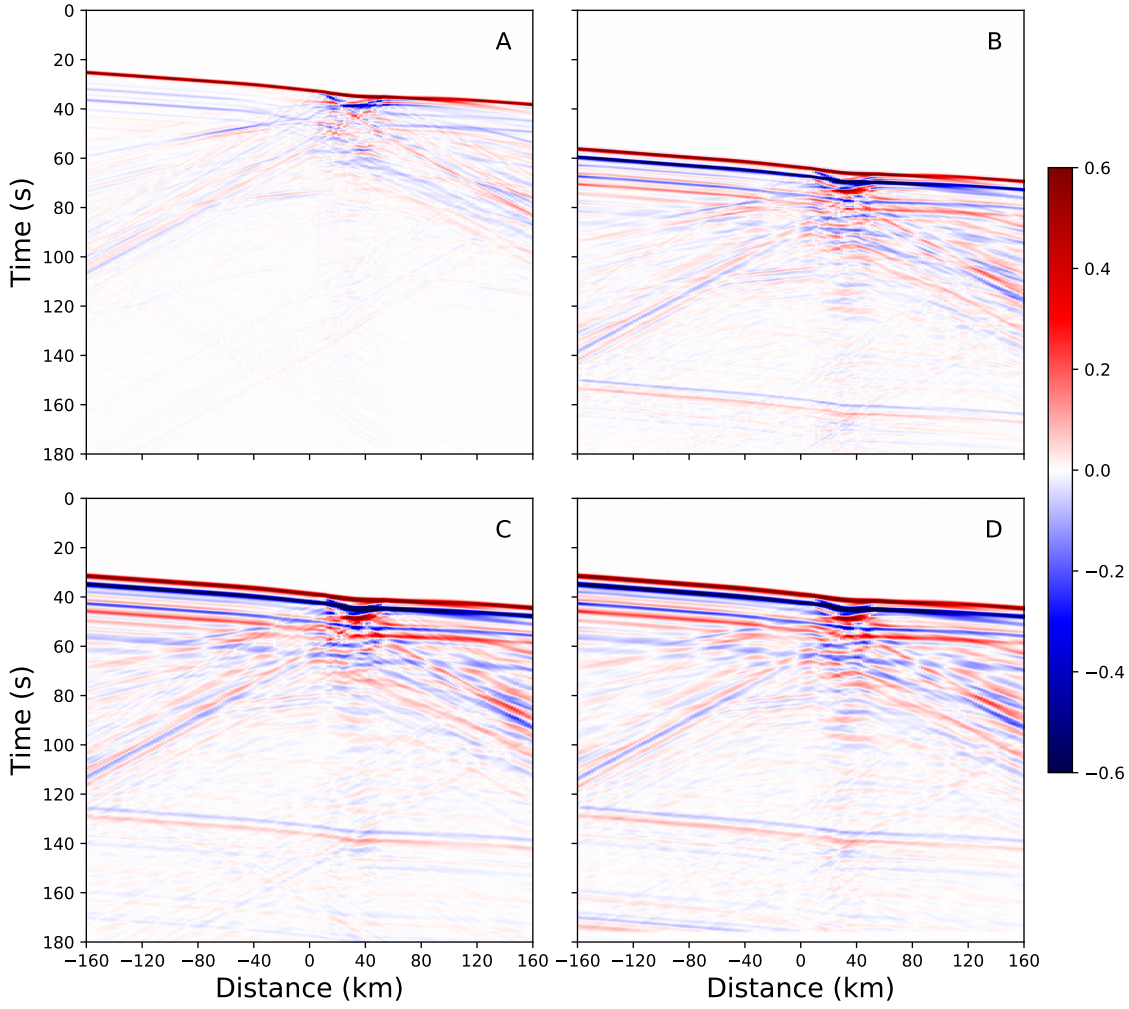

Figure 5. Same as figure 3 but for a source at 90° and 10 km depth.

4 DISCUSSION

Our simulation results have shown that the computation of the incident wavefield with AxiSEM represents by far the most time consuming step in injection methods. However, such computations are now easily affordable, even at periods as low as 2-3 s.

The first and perhaps most obvious limitation of FK compared to AxiSEM is that it cannot account for the curvature of the wavefront and of the Earth. However, for regional scale problems, i.e. considering grid sizes limited to a few degrees, our simulations demonstrate that these effects

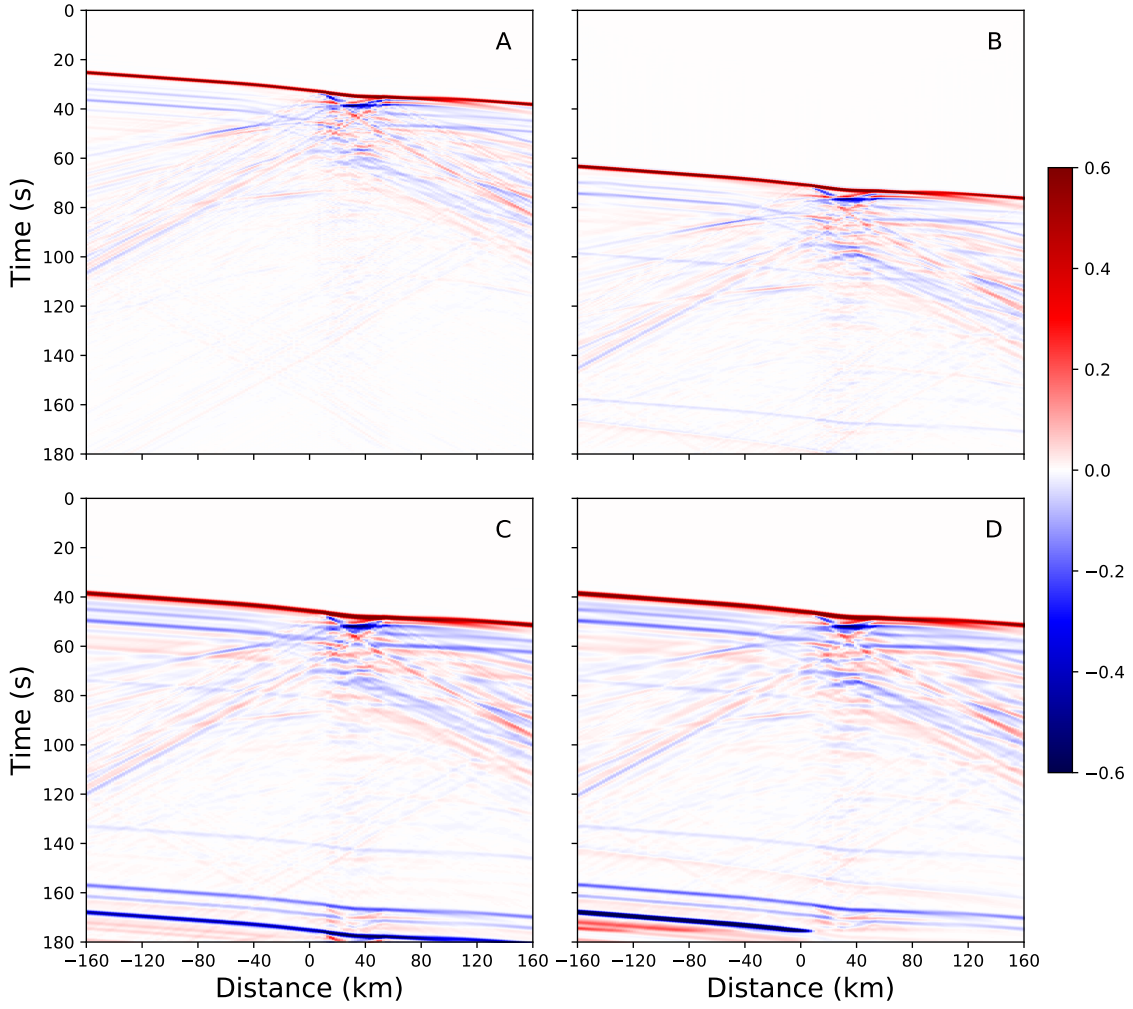

Figure 6. Same as figure 3 but for a source at 90° and 600 km depth.

are actually rather small. The variation of travel time with distance from a reference station located at epicentral distance Δ_0 is given by the Taylor expansion

$$T(\Delta) = T(\Delta_0) + \frac{\partial T}{\partial \Delta}(\Delta - \Delta_0) + \frac{1}{2}\frac{\partial^2 T}{\partial \Delta^2}(\Delta - \Delta_0)^2 \,. \tag{11}$$

The second right-hand term in (11) gives the travel time variation for a plane wave, which is directly related to its ray parameter $p = \frac{\partial T}{\partial \Delta}$. The third right-hand term quantifies the deviation from the plane wave, which results from the curvature of the Earth and of the wavefront. Figure 8 represents this travel time deviation as a function of the size of the grid, assuming $\frac{\partial^2 T}{\partial \Delta^2}$ = 0.01 s/deg^2,

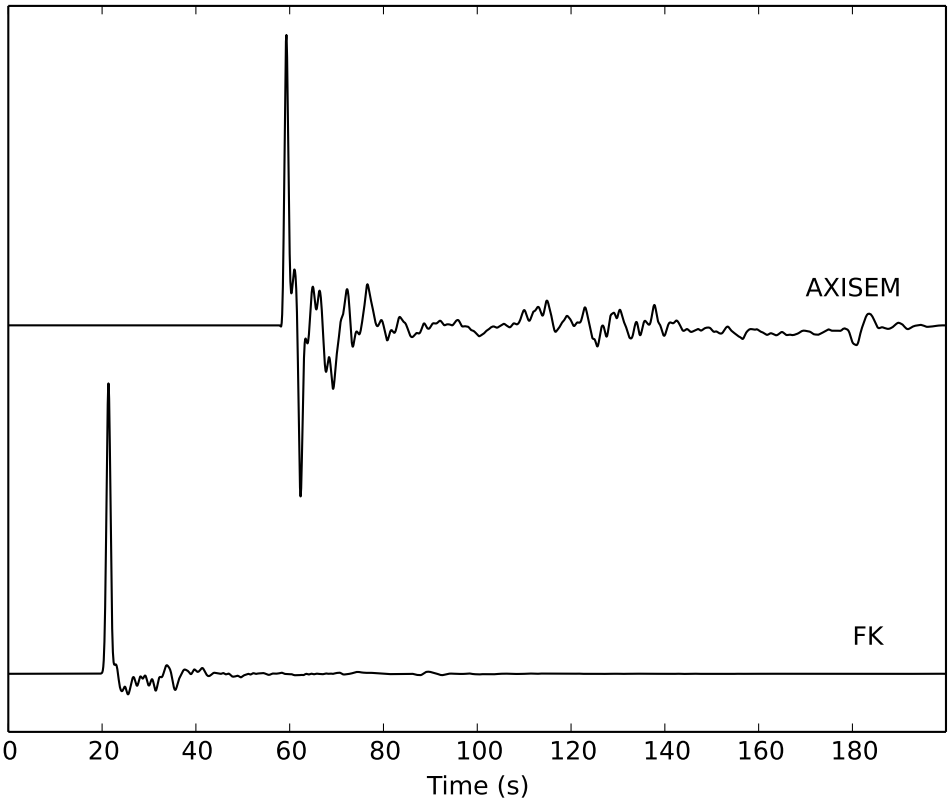

Figure 7. Average incident wavelet of synthetic seismograms computed with FK (Bottom) and AxiSEM (Top) for a source located at an epicentral distance of 30° and 10 km depth.

a typical value for P waves at teleseismic epicentral distances (30-90 degrees). For example, considering a 4°x4° grid size, the maximum travel time difference between FK and AxiSEM will be around 0.02 s. For waveform inversion problems, which typically exploit the 5-20 s period range, this time deviation is thus expected to have a negligible effect. Obviously, when moving to shorter periods and larger regional domains, the intrinsic limitations of FK will become a more serious issue.

As stated earlier, an important ingredient in the recipes of synthetic seismogram computation and full waveform inversion is the source wavelet. This source wavelet is usually estimated from the observed waveforms (Wang et al. 2016; Beller et al. 2018b). The principle is to deconvolve the vertical component of synthetic seismograms computed with an impulsive source (for example a Gaussian), which can be seen as Green's functions, from the observed vertical component

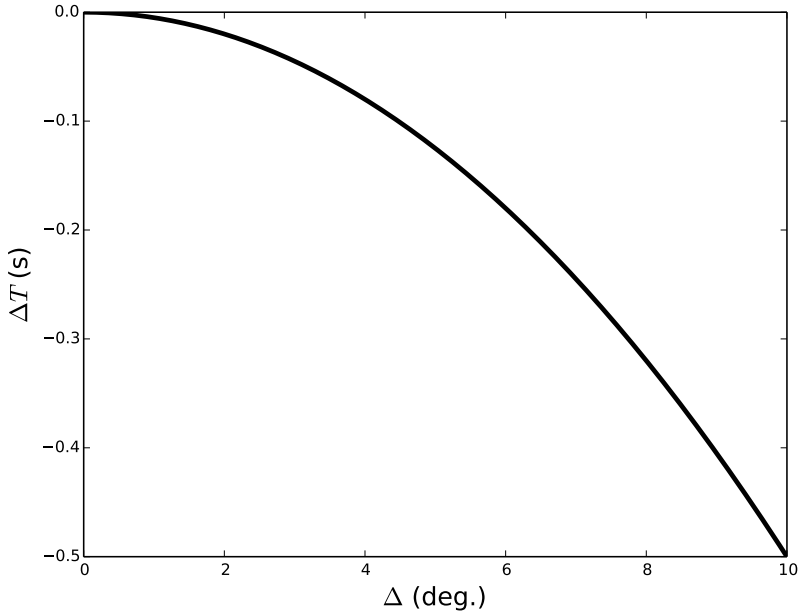

Figure 8. Travel time deviation from the plane wave assumption produced by wavefront and Earth curvature, as a function of distance from the center of the regional mesh. To compute this curve we have assumed $\frac{\partial^2 T}{\partial \Delta^2} = 0.01$ s/deg^2, a representative value for teleseismic P waves.

waveforms. This gives us apparent source wavelets at each station which usually show some differences owing to the strong crustal heterogeneity. Aligning and stacking these wavelets to extract their coherent part provides a reasonable approximation of the source wavelet. Indeed, when this source wavelet is convolved with the synthetic seismograms, the vertical component of teleseismic P records is strongly correlated to the observed data. This wavelet estimation procedure absorbs most of the source-side complexities that may affect the seismic waveforms. For example, depth phases (pP and sP) have slownesses that are very close to the one of the direct P wave. Therefore, the average source wavelet will contain the mixed contributions of both direct and depth phases. By the same token, Christensen & Ruff (1985) have shown that for shallow events (depth < 30 km), the change in Green's functions caused by an incorrect hypocentral depth can always be compensated by changes in the source time function, producing the same final seismograms.

The similarity between synthetic seismograms computed with FK convolved with the average AxiSEM P wavelet and synthetic seismograms computed with AxiSEM convolved with the average FK P wavelet (Figures 3-6C,D) suggests that in most cases, a single incident plane wave

provides a good approximation of the incident wavefield. The source-side complexities that are present in the AxiSEM computation would simply be absorbed by the source wavelet estimation if the Green's functions were computed with FK. The only problem that may arise is when a secondary phase with a slowness different from the direct P wave is present in the analysed time window. This is the case in figure 3, where the PP wave and related multiples arrive ∼50-70 s after the P wave. Another potentially disrupting phase is PcP in the 60-80° distance range. However, in practice, this phase is often barely visible on real data owing to its small amplitude compared to the direct P wave. Therefore, our numerical tests suggest that computing the incident P wavefield with the frequency-wavenumber method should provide synthetic seismograms that are in most cases accurate enough for full waveform inversion of teleseismic waveforms, provided that the data set has been carefully selected. In practice, since data sets built for full waveform inversion cover a broad range of source backazimuths and epicentral distances, the remaining biases that could come from approximating the incident wavefields with planar waves should cancel out and one can thus expect a limited impact on the inversion results. In any case, since AxiSEM computations, while more demanding, can now be performed routinely on moderate size clusters even at periods as short as a few seconds, the AxiSEM injection method is thus probably currently the best choice for teleseismic regional scale full waveform inversion. Therefore, we anticipate that the most promising applications of the FK injection method will come from high frequency ($f \geq 1$ Hz) applications at the local scale, typically geotechnical or site effects studies, for which the curvature of the wavefronts produced by distant sources can be safely neglected.

Note again that we have here only considered teleseismic P waves, as in our first full waveform imaging studies (Monteiller et al. 2015; Wang et al. 2016; Beller et al. 2018a,b). However, our hybrid methods can also be used to model teleseismic SH and SV waveforms and in principle it should be straightforward to extend the full waveform inversion method to shear waves. A recent study has demonstrated the importance of inverting simultaneously P and S waveforms for imaging upper mantle seismic anisotropy (Beller & Chevrot 2020).

5 CONCLUSIONS

We have developed and optimized a new toolkit for the computation of synthetic seismograms of short period teleseismic body waves in regional 3D models by coupling the FK or AxiSEM methods with the spectral-element code SPECFEM3D_Cartesian. Detailed comparisons of teleseismic wave fields computed with these two methods have shown that for short-period P waves (T $>$ 2 s) and for regional domains not larger than a few degrees, approximating the incident wave field with a single planar wave usually provides reasonably accurate modeling results. Nevertheless, since the extra cost of using AxiSEM is now easily affordable, we believe that AxiSEM currently represents the best choice to compute synthetic seismograms with teleseismic hybrid numerical methods, unless high frequencies (f $\geq$ 1 Hz) are considered.

6 DATA AND RESSOURCES

AxiSEM and FK coupling methods are part of SPECFEM3D_Cartesian software, available at https://gitlab.com/Seismic_Imaging/RegHyM.

7 ACKNOWLEDGEMENTS

We thank Yder Masson and Qinya Liu for their insightful and constructive reviews. This study was supported by the ANR AAPG program (project CLEARVIEW, ANR-17-CE23-0022) and the OROGEN research project, a tripartite partnership between the CNRS, TOTAL and BRGM. This research also received funding from the European Union's Horizon 2020 research and innovation programme under the ChEESE project, grant agreement No. 823844. This work was granted access to the HPC resources of IDRIS under the allocation A0070411066 made by GENCI.

REFERENCES

Beller, S. & Chevrot, S., 2020, Probing depth and lateral variations of upper-mantle seismic anisotropy from full-waveform inversion of teleseismic body-waves, *Geophys. J. Int.*, **222**, 352–387.

Beller, S., Monteiller, V., Combe, L., Operto, S., & Nolet, G., 2018, On the sensitivity of teleseismic full-waveform inversion to earth parametrization, initial model and acquisition design, *Geophys. J. Int.*, **212**, 1344–1368.

Beller, S., Monteiller, V., Operto, S., Nolet, G., Paul, A., & Zhao, L., 2018, Lithospheric architecture of the South-Western Alps revealed by multiparameter teleseismic full-waveform inversion, *Geophys. J. Int.*, **212**(2), 1369–1388.

Bielak, J. & Christiano, P., 1984, On the effective seismic input for non-linear soil-structure interaction systems, *Earthquake Eng. Struct. Dyn.*, **12**, 107–119.

Capdeville, Y., Chaljub, E., Vilotte, J. P., & Montagner, J. P., 2003, Coupling the spectral element method with a modal solution for elastic wave propagation in global earth models, *Geophys. J. Int.*, **152**, 34–67.

Castle, J. C. & Creager, K. C., 1998, Topography of the 660-km seismic discontinuity beneath Izu-Bonin: Implications for tectonic history and slab deformation, *J. Geophys. Res.*, **103**, 12511–12527.

Chevrot, S., Favier, N., & Komatitsch, D., 2004, Shear wave splitting in three-dimensional anisotropic media, *Geophys. J. Int.*, **159**, 711–720.

Christensen, D. H. & Ruff, L. J., 1985, Analysis of the trade-off between hypocentral depth and source time function, *Bull. Seismol. Soc. Am.*, **75**(6), 1637–1656.

Clayton, R. & Engquist, B., 1977, Absorbing boundary conditions for acoustic and elastic wave equations, *Bull. Seismol. Soc. Am.*, **67**, 1529–1540.

Frigo, M. & Johnson, S. G., 2005, The design and implementation of FFTW3, *Proc. IEEE*, **93**(2), 216–231.

Kawai, K., Takeuchi, N., & Geller, R. J., 2006, Complete synthetic seismograms up to 2 Hz for transversely isotropic spherically symmetric media, *Geophys. J. Int.*, **164**, 411–424.

Kennett, B. L. N., Engdahl, E. R., & Buland, R., 1995, Constraints on seismic velocities in the Earth from traveltimes, *Geophys. J. Int.*, **122**, 108–124.

Komatitsch, D. & Tromp, J., 1999, Introduction to the spectral-element method for 3-D seismic wave propagation, *Geophys. J. Int.*, **139**, 806–822.

Komatitsch, D. & Tromp, J., 2002, Spectral-element simulations of global seismic wave propagation-I. Validation, *Geophys. J. Int*, **149**, 390–412.

Komatitsch, D., Tsuboi, S., Ji, C., & Tromp, J., 2003, A 14.6 billion degrees of freedom, 5 teraflops, 2.5 terabyte earthquake simulation on the Earth Simulator, *Proceedings of the ACM/IEEE Supercomputing SC'2003 conference*, published on CD-ROM and at www.sc-conference.org/sc2003.

Lin, C., Monteiller, V., Wang, K., Liu, T., Tong, P., & Liu, Q., 2019, High-frequency seismic wave modelling of the deep Earth based on hybrid methods and spectral-element simulations: a conceptual study,

Geophys. J. Int., **219**, 1948–1969.

Mallick, S. & Frazer, L. N., 1987, Practical aspects of reflectivity modeling, *Geophysics*, **52**(10), 1355–1364.

Masson, Y. & Romanowicz, B., 2017, Fast computation of synthetic seismograms within a medium containing remote localized perturbations: a numerical solution to the scattering problem, *Geophys. J. Int.*, **208**, 674–692.

Masson, Y. & Romanowicz, B., 2017, Box tomography: localized imaging of remote targets buried in an unknown medium, a step forward for understanding key structures in the deep Earth, *Geophys. J. Int.*, **211**, 141–163.

Monteiller, V., Chevrot, S., Komatitsch, D., & Fuji, N., 2013, A hybrid method to compute short-period synthetic seismograms of teleseismic body waves in a 3-D regional model, *Geophys. J. Int.*, **192**, 230–247.

Monteiller, V., Chevrot, S., Komatitsch, D., & Wang, Y., 2015, Three-dimensional full waveform inversion of short-period teleseismic wavefields based upon the SEM-DSM hybrid method, *Geophys. J. Int.*, **202**, 811–827.

Nissen-Meyer, T., Dahlen, F. A., & Fournier, A., 2007, Spherical-Earth Fréchet sensitivity kernels, *Geophys. J. Int.*, **168**(3), 1067–1092.

Nissen-Meyer, T., Driel, M., Stähler, S., Hosseini, K., Hempel, S., Auer, L., Colombi, A., & Fournier, A., 2014, AxiSEM: broadband 3-D seismic wavefields in axisymmetric media, *Solid Earth*, **1**, 425–445.

Roecker, S., Baker, B., & McLaughlin, J., 2010, A finite-difference algorithm for full waveform teleseismic tomography, *Geophys. J. Int.*, **181**, 1017–1040.

Rondenay, S., 2009, Upper mantle imaging with array recordings of converted and scattered teleseismic waves, *Surv. Geophys.*, **30**, 377–405.

Takeuchi, H. & Saito, M., 1972, *Methods of computational physics*, chap. Seismic surface waves, pp. 217–295, Academic Press, New York.

Tong, P., Chen, C., Komatitsch, D., Basini, P., & Liu, Q., 2014, High-resolution seismic array imaging based on an SEM-FK hybrid method, *Geophys. J. Int.*.

Tong, P., Komatitsch, D., Tseng, T. L., Hung, S. H., Chen, C. W., Basini, P., & Liu, Q., 2014, A 3D spectral-element and frequency-wavenumber hybrid method for high-resolution seismic array imaging, *Geophys. Res. Lett.*, **41**(20), 7025–7034.

Unser, M., 1999, Splines: A perfect fit for signal and image processing, *IEEE Signal Processing Magazine*, **16**(6), 22–37.

Unser, M., Aldroubi, A., & Eden, M., 1991, Fast B-spline transforms for continuous image representations and interpolation, *IEEE Trans. on Pattern Analysis and Machine Intelligence*, **13**(3), 277–285.

Unser, M., Aldroubi, A., & Eden, M., 1993, B-spline signal processing: Part I – Theory, *IEEE Trans.*

Signal Process., **41**(2), 821–832.

Unser, M., Aldroubi, A., & Eden, M., 1993, B-spline signal processing: Part II – Efficient design and applications, *IEEE Trans. Signal Process.*, **41**(2), 834–848.

Wang, Y., Chevrot, S., Monteiller, V., Komatitsch, D., Mouthereau, F., Manatschal, G., Sylvander, S., Diaz, J., Ruiz, M., Grimaud, F., Benahmed, S., Pauchet, H., & Martin, R., 2016, The deep roots of the western Pyrenees revealed by full waveform inversion of teleseismic P waves, *Geology*, **44**(6), 475–478.

Zhu, L. & Rivera, L., 2002, A note on the dynamic and static displacements from a point source in multi-layered media, *Geophys. J. Int.*, **148**, 619–627.

APPENDIX A: OPTIMIZATION OF THE INJECTION ALGORITHM

A1 Coupling optimization: cubic B-spline interpolation

The time step of the spectral-element simulation Δt needs to verify the stability condition

$$\Delta t \leq 0.3 \min \left(\frac{h}{V_p} \right) , \tag{A.1}$$

where h is the shortest distance between two neighboring mesh nodes and V_p the compressional velocity. Usually, Δt is much smaller than the dominant period of the wave and thus it would be extremely inefficient to compute and store the velocities and tractions for the injection at the SPECFEM3D_Cartesian time step.

Cubic B-splines provide a basis function to represent continuous functions. Any continuous function ϕ can be expanded in the B-spline basis as

$$\phi(x) = \sum_{k=-\infty}^{+\infty} c_k \beta^3(x-k) \tag{A.2}$$

where the c_k are the spline coefficients (Unser et al. 1991; Unser 1999) and $\beta^3(x)$ is the normalized B-spline of order 3 (Unser 1999):

$$\beta^3(x) = \begin{cases} \frac{2}{3} - \|x\|^2 + \frac{\|x\|^3}{2}, & 0 \leq \|x\| < 1 \\ \frac{(2-\|x\|)^3}{6}, & 1 \leq \|x\| < 2 \\ 0, & 2 \leq \|x\| \end{cases} \tag{A.3}$$

Given a regularly sampled signal s_k, the spline coefficients can be efficiently determined with two recursive filters (Unser et al. 1993a,b)

$$c_k^+ = s_k + \alpha c_{k-1}^+, (k = 2, ..., K) \tag{A.4}$$

$$c_K^+ = -\frac{\alpha}{1-\alpha^2}(2c_K^+ - s_K) \tag{A.5}$$

$$c_k^- = \alpha \left(c_{k+1}^- - c_k^+ \right), (k = K-1, ..., 1), \tag{A.6}$$

with $\alpha = \sqrt{3} - 2$. The seed value c_1 is computed by imposing a mirror boundary condition at the beginning of the sequence. This algorithm is extremely efficient because it only requires two additions and two multiplications per sample point. Another advantage is that all the operations are performed in-place, thus the algorithm is also memory-efficient, leading to minimum i/o. Once

the spline coefficients are computed, it is then easy to resample the times series using (A.2) and (A.3).

A2 FK Optimization

We have modified the original FK algorithm developed by Tong et al. (2014a) to improve its efficiency. We first performed standard low level optimizations such as extractions of if statements from loops. Since FK works in the frequency domain, the incident tractions and velocities computed with FK thus need to be transformed in the time domain. This requires a large number of Fast Fourier Transforms (FFT), because this needs to be done for the three components of both tractions and velocities on all the GLL nodes located on the external boundaries of the spectral element mesh. These FFT have been accelerated by calling the routines in the FFTW library (Frigo & Johnson 2005). Finally we reorganized the FK algorithm itself, in order to exploit the symmetries of the problem and minimize the number of operations. Figure A1 represents the original FK flowchart from Tong et al. (2014a). In this implementation, the propagator matrix was recomputed for each GLL node and each frequency (cf. Appendix A in Tong et al. (2014a)). This implementation is not optimal since the propagation matrices are the same for all the nodes located in the same layer. We thus reorganised the FK computations as summarized in Figure A2. We now compute and store, for each frequency, the propagation matrices N_i corresponding to each layer i in the 1D model. We then loop on each GLL boundary node and compare the depth of the current point with the depth of the previous one. If the depth is different, we compute and store in the memory the complete propagation matrices at each frequency and compute the frequency fields. If the depth is the same, we load the propagation matrices and the frequency fields. This method provides a good trade-off between computational efficiency and memory pressure as we are only storing propagation matrices at each frequency for a given depth at a time, and that in general points at a given depth are consecutive. Taken together, these optimizations allowed us to reduce the FK computation time by a factor of 5.

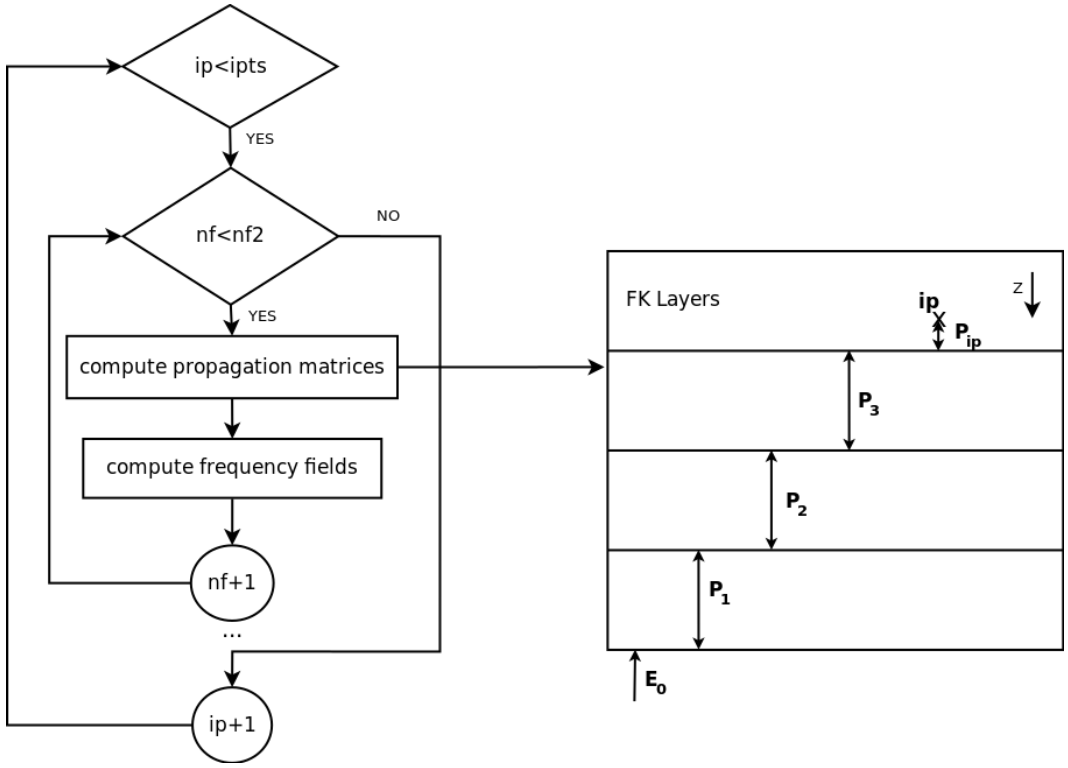

Figure A1. Original FK computation flowchart. A first loop is performed over the $ipts$ nodes on the edges of the mesh inside which a second loop is performed over the $nf2$ frequencies.

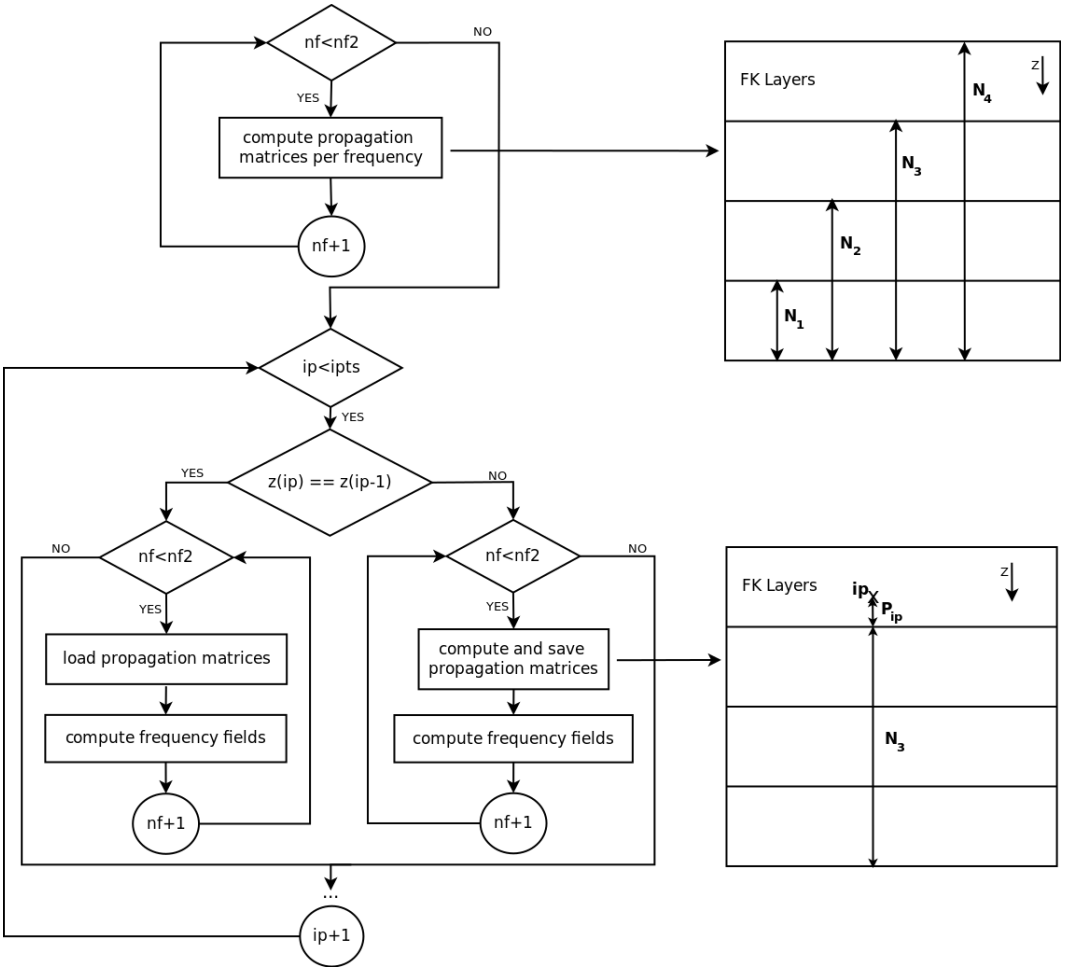

Figure A2. Optimized FK computation flowchart

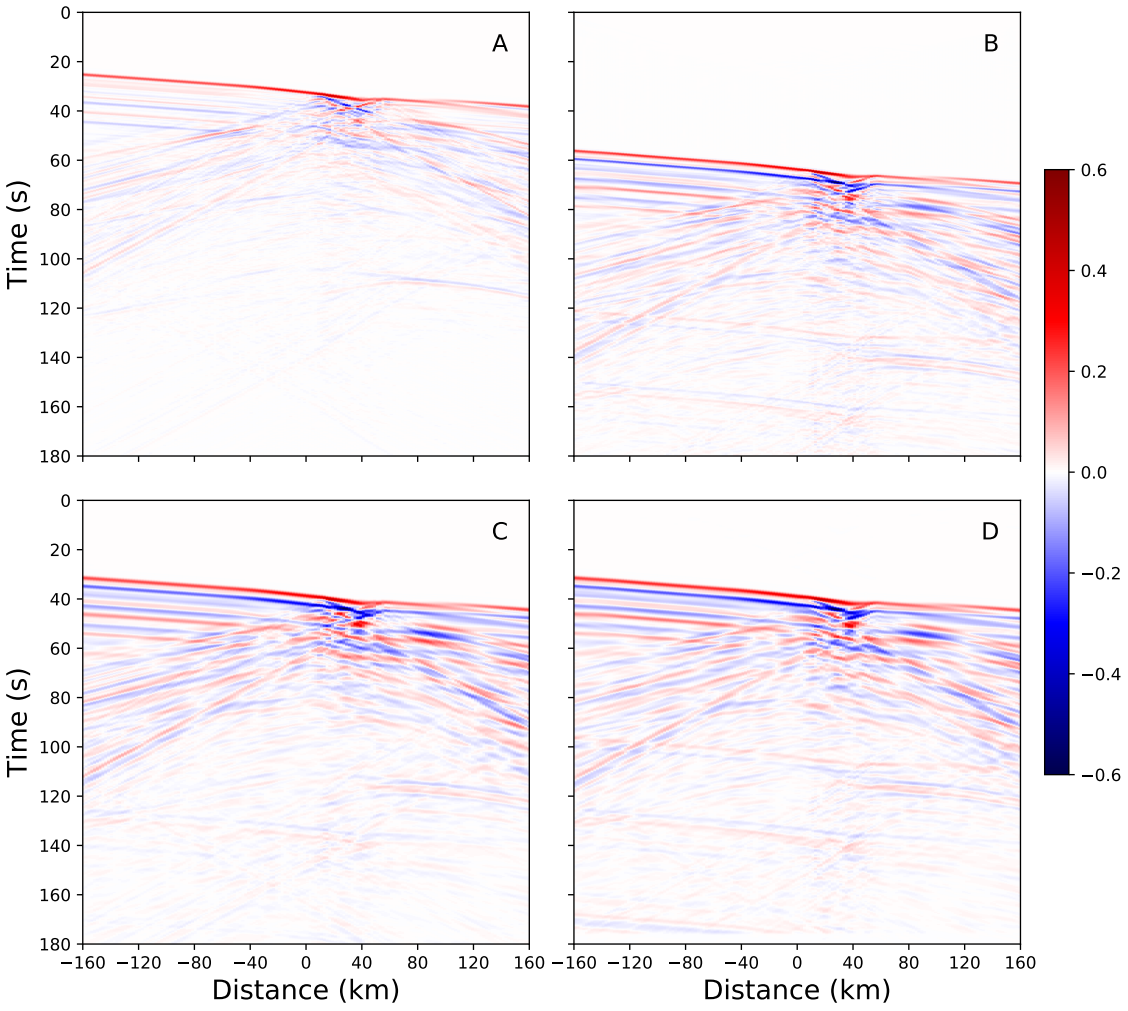

[h]

Figure A3. Same as figure 3 but for a source at 90° and 10 km depth.

A3 Radial components

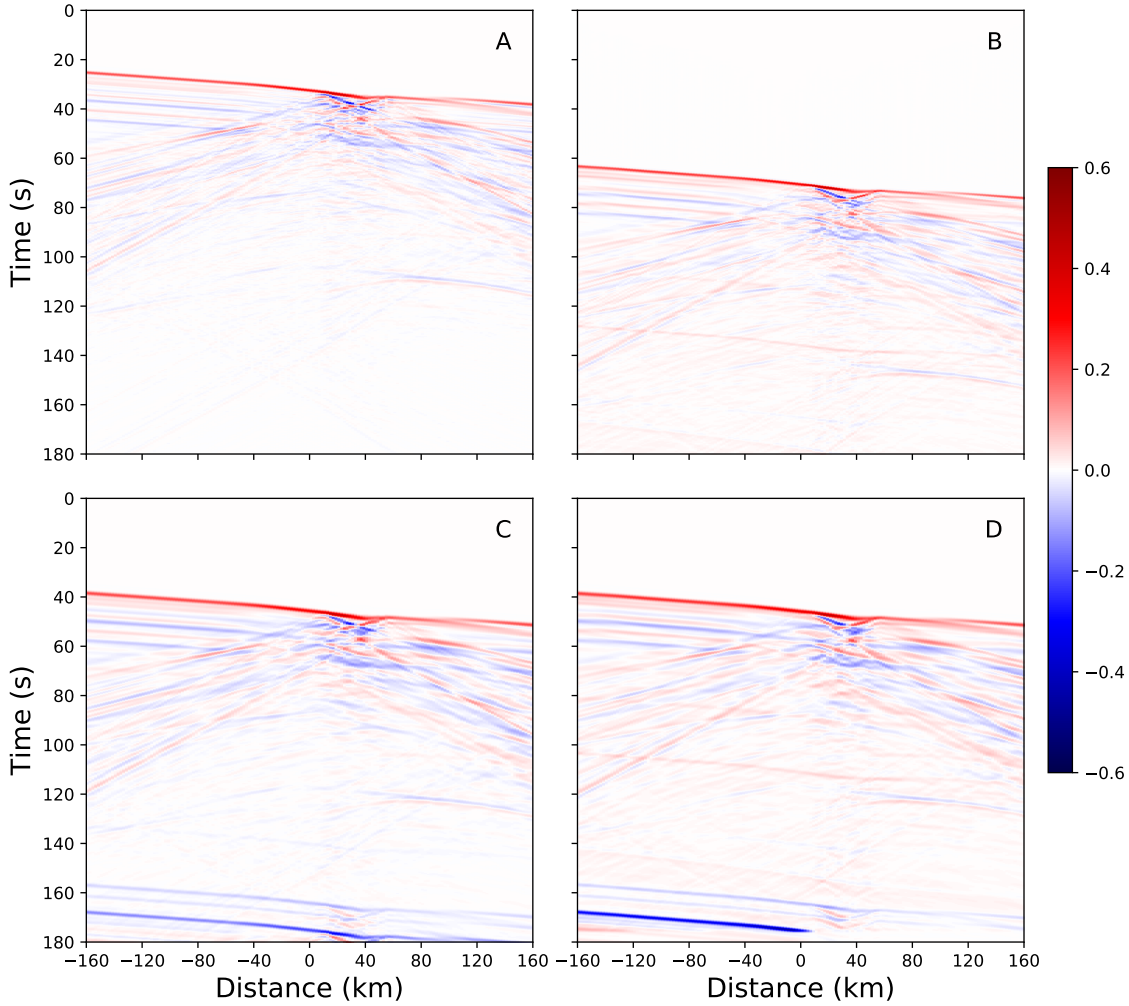

Figure A4. Same as figure 3 but for a source at 90° and 600 km depth.

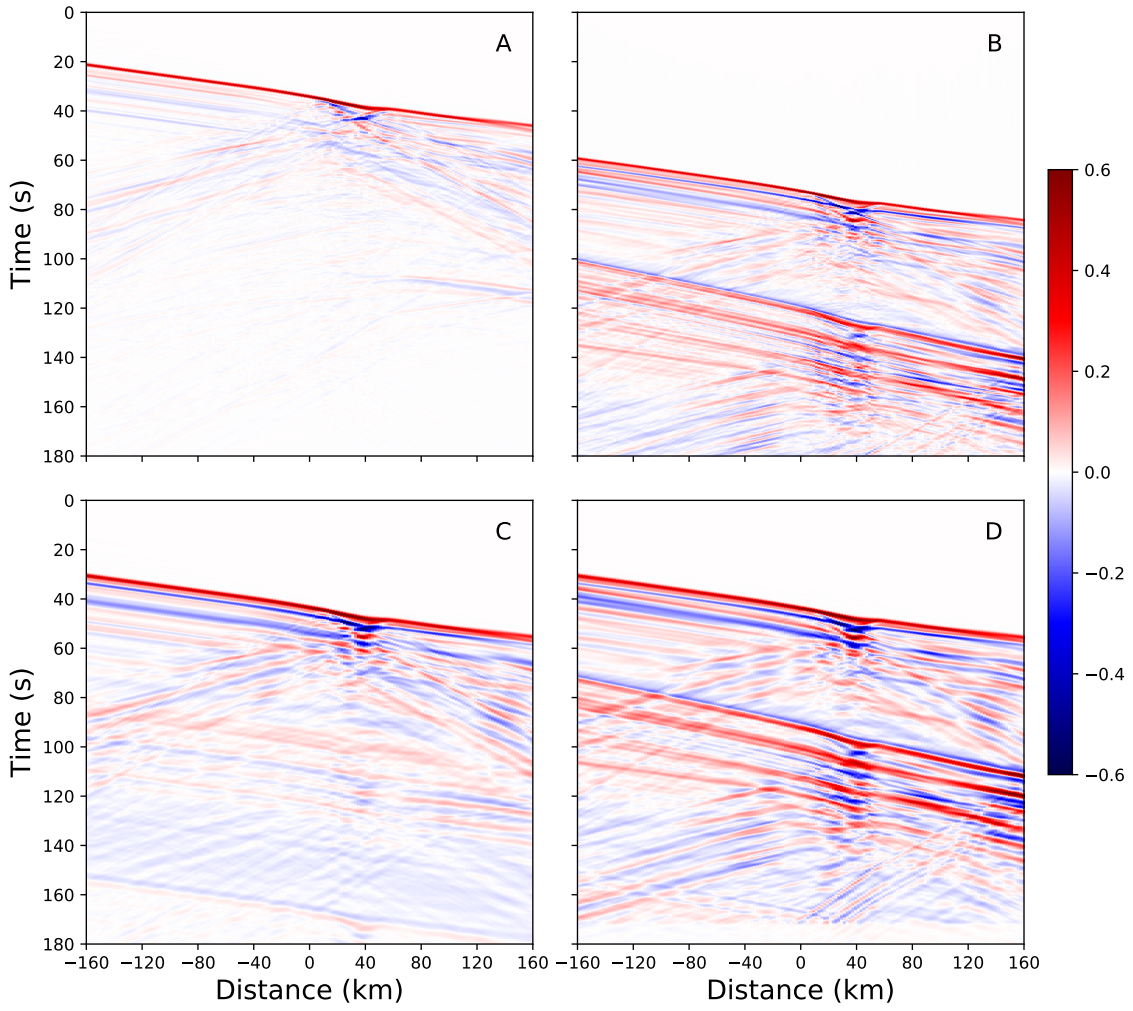

Figure A5. Radial component of synthetic seismograms computed with FK (A) and AxiSEM (B) for a source located at an epicentral distance of 30° and 10 km depth. Same seismograms, but convolved with the average Axisem wavelet (C) and with the average FK wavelet (D).

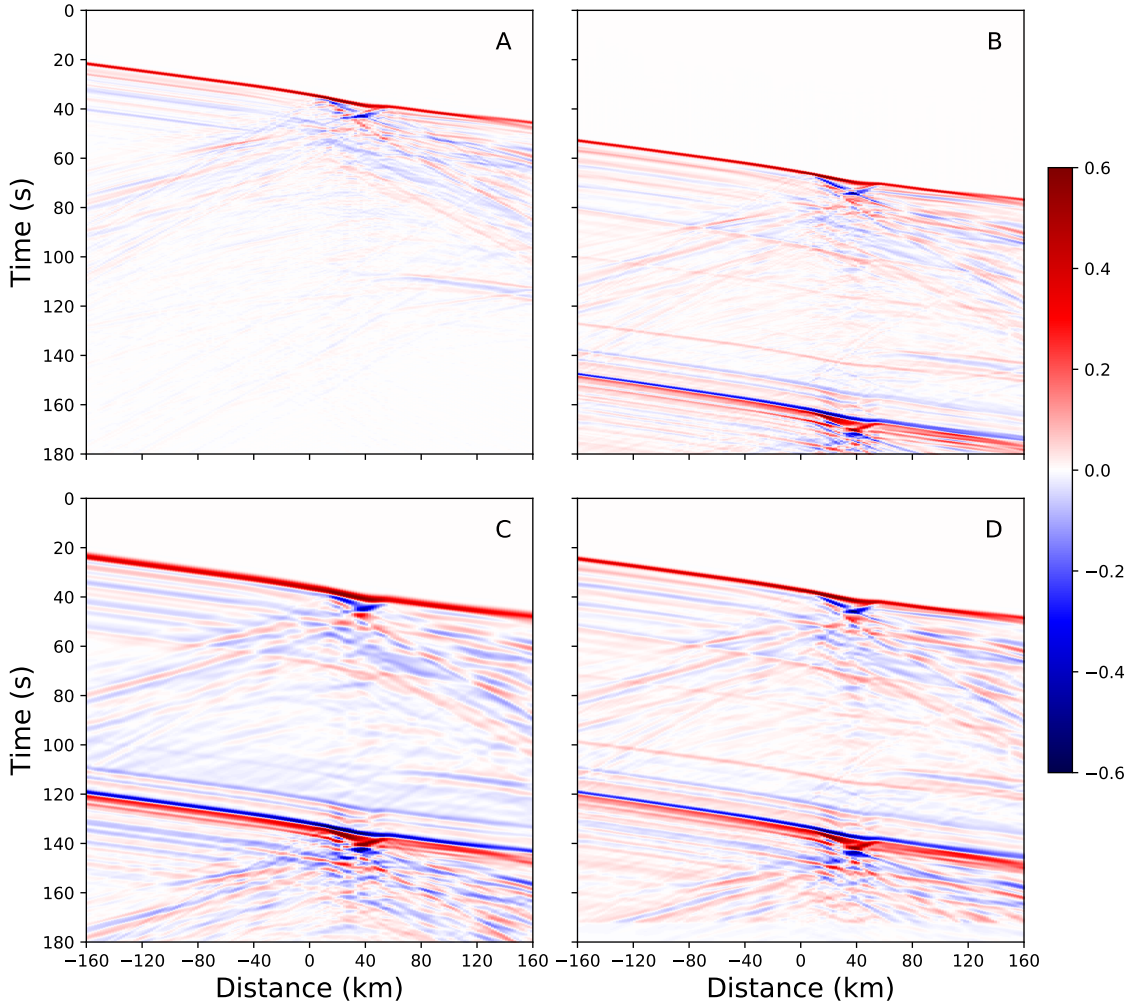

Figure A6. Same as figure 3 but for a source at 600 km depth.